La Société Savante
de l'Aéronautique et de l'Espace

*57th 3AF International Conference*
*on Applied Aerodynamics*
*29 — 31 March 2023, Bordeaux – France*

**AERO2023-16-SABNIS**

# EXPERIMENTAL INVESTIGATION OF TRANSONIC EXTERNAL FAN COWL SEPARATION

**K. Sabnis [(1)] *, L. Boscagli [(2)], H. Babinsky [(1)], D. MacManus [(2)] and C. Sheaf [(3)]**
[(1)] *Department of Engineering, University of Cambridge, Cambridge, CB2 1PZ, UK*
[(2)] *Centre for Propulsion Engineering, Cranfield University, Cranfield, MK43 0AL, UK*
[(3)] *Installation Aerodynamics, Rolls–Royce plc, Derby, DE24 8BJ, UK*
* Corresponding author: *ks648@cam.ac.uk*

## ABSTRACT

When a civil aircraft engine is shut down during the cruise phase of flight and thus begins to windmill, a supersonic region forms on the external surface of the fan cowl. The terminating normal shock can separate the turbulent boundary layer developing on this external surface. A series of experiments are performed in a quasi-two-dimensional wind tunnel rig to investigate the influence of various parameters on this flow problem. As the engine mass-flow rate is reduced, an increase in normal shock strength results in the onset of flow separation which thickens the boundary layer developing on the external fan cowl surface by a factor of three. A reduction in incoming Mach number from the nominal value of 0.65 to 0.60 weakens the shock wave and thus delays flow separation. If the incoming boundary layer is laminar rather than turbulent, the normal shock Mach number is observed to increased by 10%. Despite the stronger shock, no significant flow separation can be detected even for the lowest engine mass-flow rates studied and the external nacelle surface boundary layer is measured to be thinner than for the turbulent case.

## 1. INTRODUCTION

The flow field around aircraft engine nacelles is generally well understood for design conditions such as cruise. Fan cowl geometries are optimised for aerodynamic efficiency at these conditions, with no significant flow separation on the internal or external nacelle surfaces [1]. However, the flow separation behaviour in off-design scenarios, such as crosswind or engine windmilling, has not been studied as extensively and the detailed aerodynamics remains relatively unknown. For high-bypass ratio engines currently in service, the design margins to ensure that significant separation is avoided are well understood.

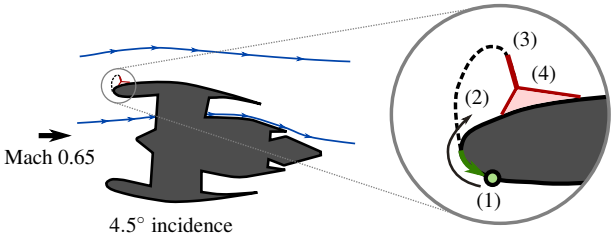


(1) stagnation point moves inboard
(2) curvature causes flow acceleration to supersonic
(3) supersonic region terminates in normal shock
(4) shock pressure rise separates boundary layer

Figure 1: Schematic of the flow separation mechanism in response to a reduced engine mass-flow rate in diversion windmilling conditions.

However, in order to satisfy environmental targets under the European Commission's FlightPath 2050 vision [2], the aviation industry is actively developing ultra high-bypass ratio (UHBPR) engines which are more efficient but also have substantially larger fans. To minimise the drag penalty from increased wetted area, UHBPR engine nacelles need to be compact, with high local curvature at the lip, and are thus more prone to flow separation [3]. An off-design scenario which is particularly relevant to UHBPR engine nacelles concerns windmilling after engine shut down during cruise. In this situation, termed "diversion windmilling", the mass-flow rate through the engine is reduced. Within the context of this work, the nacelle incidence angle is 4.5 degrees and the aircraft is slowed from its cruise operating condition such that the nominal incoming Mach number is 0.65.

Under diversion windmilling conditions, Fig. 1 shows that the highly-curved lip geometry causes a local super-

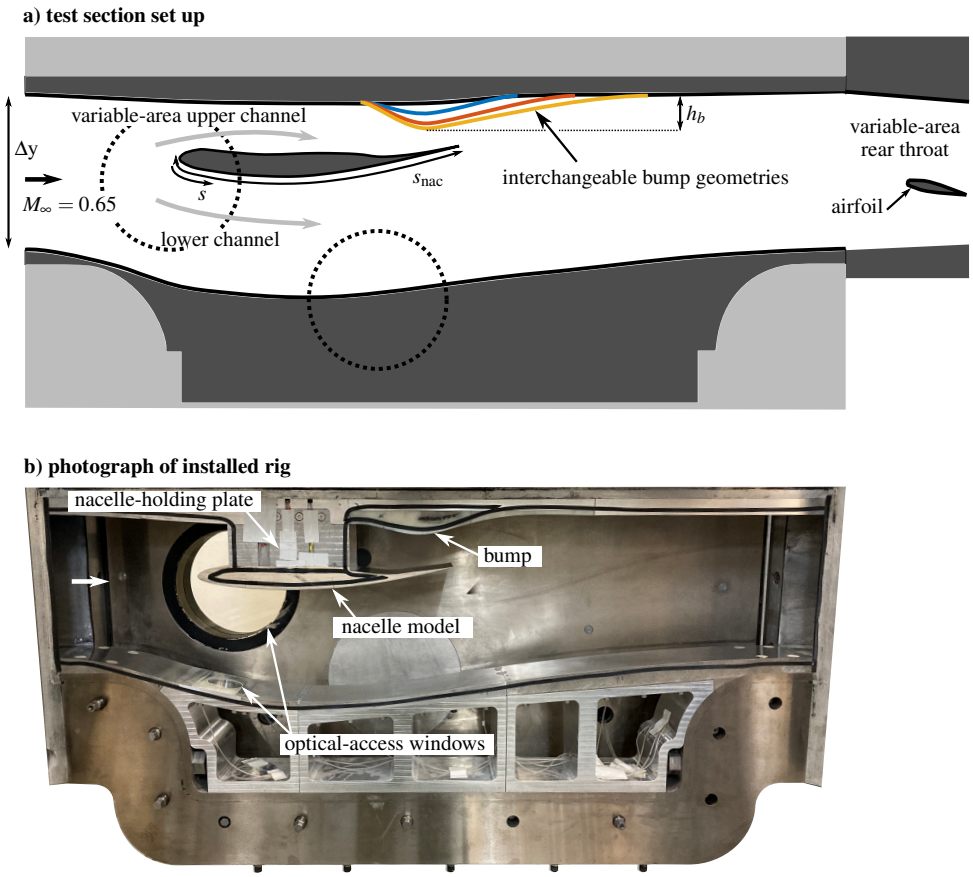


Figure 2: a) Detail of wind tunnel test section; b) photograph of installed rig.

sonic region to form on the outside of the nacelle and the terminating normal shock wave can separate the external fan-cowl boundary layer [4]. This flow detachment can subsequently have a negative impact on the aerodynamic performance of the aircraft. Nevertheless, the physical mechanisms underlying shock-induced separation during windmilling remain poorly understood. This limitation is compounded by the inability of RANS CFD methods typically used in industry to reliably predict the onset of flow detachment, the scale of separation, or the effect on the external fan cowl boundary layer.

In order to address this lack of understanding, a quasi-two-dimensional transonic test rig has been developed to replicate the external fan cowl aerodynamics from a full-scale three-dimensional nacelle. The current paper studies the diversion windmilling flow field for three different equivalent engine mass-flow rates. The effect of incoming Mach number is also assessed by considering a case with reduced Mach number, $M_\infty = 0.60$. The rig can achieve a maximum Reynolds number based on lip thickness, $\mathrm{Re}_t$, of around $2.1 \times 10^6$. Whilst this value is higher than many similar experimental facilities, the rig Reynolds number is nevertheless smaller than the full-scale scenario by a factor of three. To account for this difference, boundary-layer transition is achieved by artificial tripping. The current paper compares these results with an equivalent laminar case to ascertain the influence of boundary-layer state on the shock-induced separation.

## 2. RESEARCH METHODOLOGY

### 2.1 Wind tunnel rig

The experimental rig used in the current study is installed into a blowdown transonic wind tunnel at the University of Cambridge. The facility is driven from a high-pressure reservoir through a settling chamber. The flow then passes through a 18:1 area ratio contraction with a round-to-rectangular transition before entering the test section shown in Fig. 2. The stagnation pressure is set at $204 \pm 1$ kPa and the stagnation temperature is measured to be $302 \pm 5$ K. The test section, which is 114 mm wide and 1200 mm long, consists of an underlying structure onto which custom liner blocks, which define the flow path, are fitted.

The detailed design of the rig shown in Fig. 2a is set out in Ref. [5] and so only a brief summary is included here for completeness. A 1/14th scale model of a nacelle is installed within the flow path, suspended from the upper wall by plates on each sidewall (Fig. 2b). The

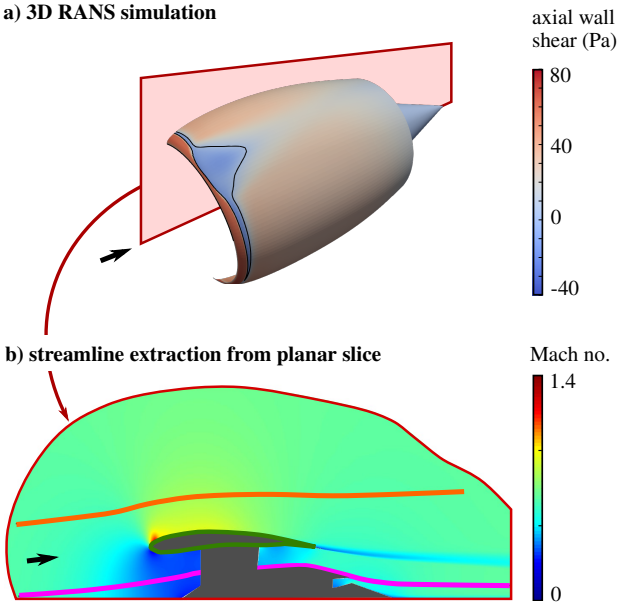


Figure 3: Schematic generation of the rig geometry for diversion windmilling: a) 3D RANS simulations of the entire nacelle; b) streamlines from a slice through the vertical plane. From Ref. [5].

chordwise coordinate, $s$, is defined from the nacelle lip highlight. This nacelle model is based on a representative 3D non-axisymmetric baseline nacelle for a long-range aircraft. The geometry of this model is equivalent to the top aeroline from this full-scale 3D design which optimises drag whilst ensuring acceptable aerodynamic performance in off-design conditions, including diversion windmilling [6]. Due to structural constraints, the model is installed in an inverted configuration such that the bottom corresponds to the external fan cowl surface and the top of the model is internal to the nacelle. The model consists of an additively-manufactured resin sleeve which fits onto a steel core that provides structural rigidity.

The geometry of the upper wall in Fig. 2 is based on a planar slice through 3D RANS computations of the full-scale nacelle under diversion windmilling conditions, as shown in Fig. 3. The contour of this wall is defined by a streamline internal to the aircraft engine from these computations. The geometry of the lower wall in Fig. 2 is determined using a parametric design approach which uses RANS computations of the wind tunnel flow path to achieve a flow field that is representative of the full-scale 3D nacelle. Specifically, the lower wall contour is chosen such that the pressure distribution imposed on the nacelle model matches the equivalent values on the external fan cowl surface of a three-dimensional nacelle during diversion windmilling. The tunnel walls are sufficiently far away from the nacelle model that they are not expected to influence the flow on the external fan cowl surface under the conditions investigated in the current study.

It is desirable to reproduce different engine mass-flow rates within the rig, which correspond to different degrees of windmilling severity. This is achieved by noting that the nacelle model splits the wind tunnel into two channels, where the upper channel corresponds to flow internal to the engine and the lower channel represents the external flow. Therefore, variations in engine mass-flow rate are replicated by adjusting the mass-flow split between these two channels. To do so, the upper wall is modified by installing a series of interchangeable variable-height bumps, shown in Fig. 2. These bumps restrict the flow through the upper channel, thus modifying the mass-flow split between the two channels. In this study, three mass-flow split cases are considered with values of bump height normalised by test-section entry height, $h_b/\Delta y = 0.159$, 0.194 and 0.227 which represent mild, moderate and severe windmilling, respectively. Based on RANS computations of the wind tunnel flow path, the intermediate case is expected to correspond roughly to the onset of shock-induced separation [5].

Figure 2a shows an airfoil installed downstream of the test section. The flow here is choked, and thus the area ratio between this point and the entry to the test section defines the tunnel entry Mach number. By varying the incidence angle of the airfoil and thus the area of the choked region, the incoming Mach number can be controlled. The current study considers two entry Mach numbers, the nominal value for a diversion windmilling scenario, $M_\infty = 0.650 \pm 0.002$ and a reduced value of $M_\infty = 0.600 \pm 0.002$.

Despite the 1/14th physical scale of the nacelle model, the fact that the facility is pressurised means that the Reynolds number is only a factor of three lower than the full-scale value. Nevertheless, a comparison between transitional RANS computations of the full-scale nacelle and of the wind tunnel flow path suggests that there is a difference between the two flow fields. The shock–boundary-layer interaction (SBLI) for the full-scale nacelle is expected to be turbulent whereas the lower Reynolds number wind tunnel rig is predicted to feature a laminar interaction [5]. This prediction is confirmed by infrared thermography images of the external fan cowl surface (Fig. 4a), which feature a temperature peak at the normal shock wave characteristic of a laminar interaction [7].

Therefore, in order to replicate the turbulent interaction seen in the real scenario, the wind tunnel model is modified to increase the surface roughness in a small region around the leading edge from 2 microns to 30 microns in order to promote transition. Figure 4b demonstrates that this approach is successful, since the temperature peak from Fig. 4a is replaced with a single temperature rise that is representative of a turbulent interaction [7]. This locally-roughened model is therefore used for the current study in order to best replicate full-scale diver-

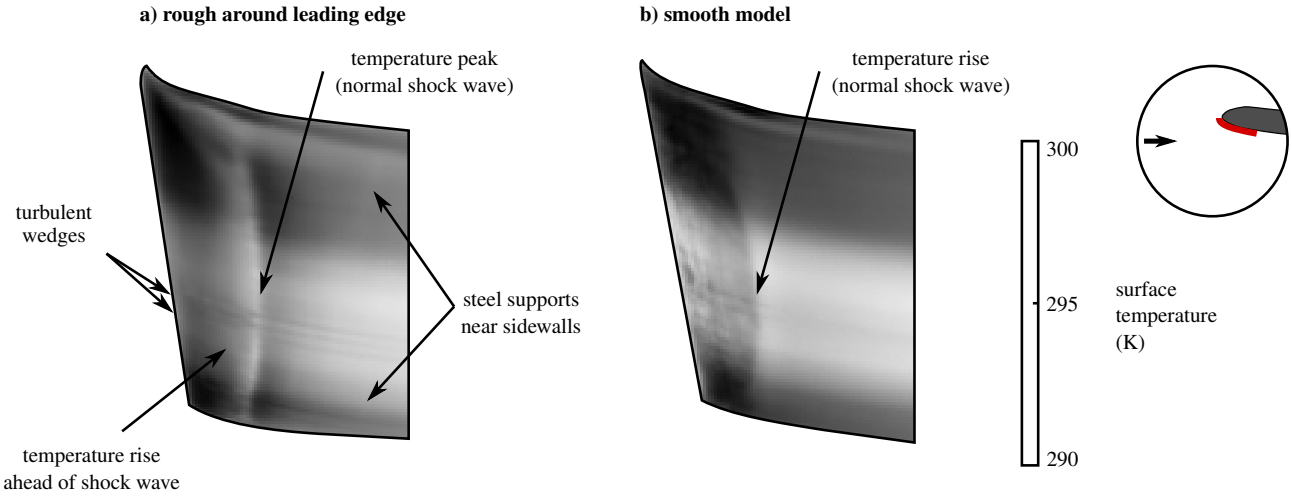


Figure 4: Temperature distribution on the external fan cowl surface, determined using infrared thermography for $h_b/\Delta y = 0.194$ and $M_\infty = 0.65$.

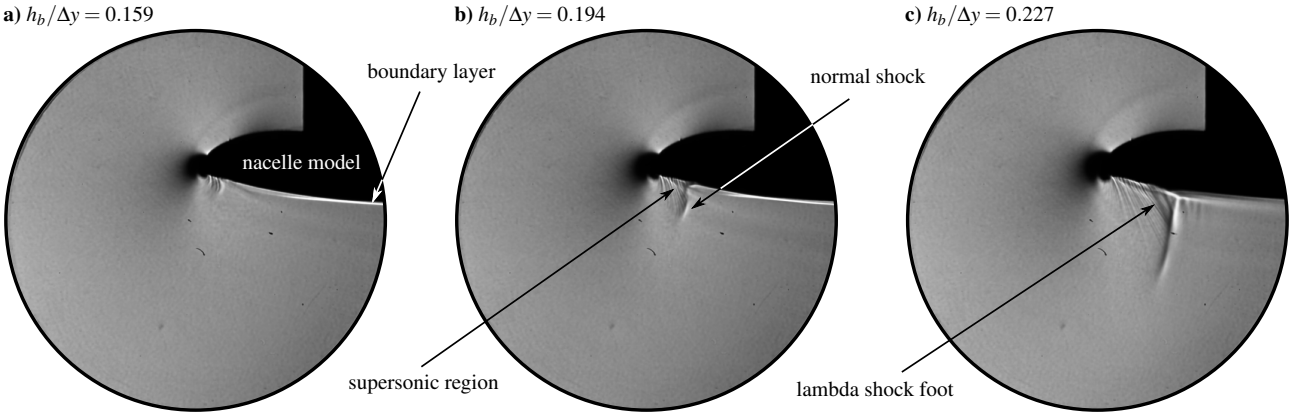


Figure 5: Schlieren images for different bump heights corresponding to variations in equivalent engine mass-flow rate.

sion windmilling scenarios. However, comparisons are also made against equivalent measurements on a fully-smooth model (corresponding to the laminar interaction in Fig. 4a) in order to provide insight into the influence of incoming boundary-layer state.

## 2.2 Experimental techniques

The infrared camera used to determine model surface temperatures in Fig. 4 is a liquid nitrogen-cooled FLIR SC7300 with an integration time of 160 µs and frame rate of 50 fps. A z-type schlieren system with a horizontal knife-edge enables visualisation of spanwise-averaged density gradients. Schlieren images are captured at 6400 frames per second using a Photron Fastcam Nova S6 camera, with an exposure time of 1.6 µs.

Steady-state surface pressure measurements are conducted using about fifty 0.3 mm diameter static pressure taps connected to a differential pressure transducer (error: ±1%) [8]. To determine surface pressure distri-

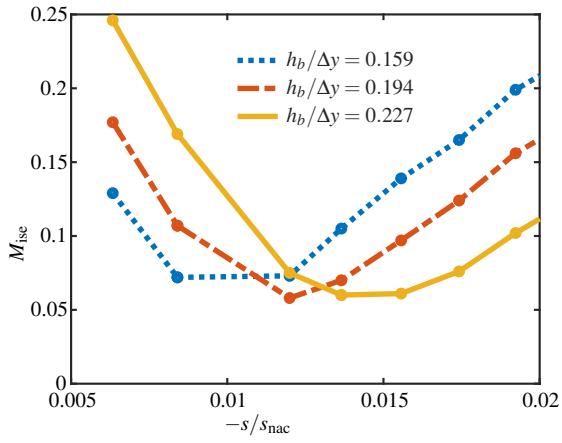


Figure 6: Pressure distribution on the internal nacelle surface around the stagnation point for different bump heights corresponding to variations in equivalent engine mass-flow rate.

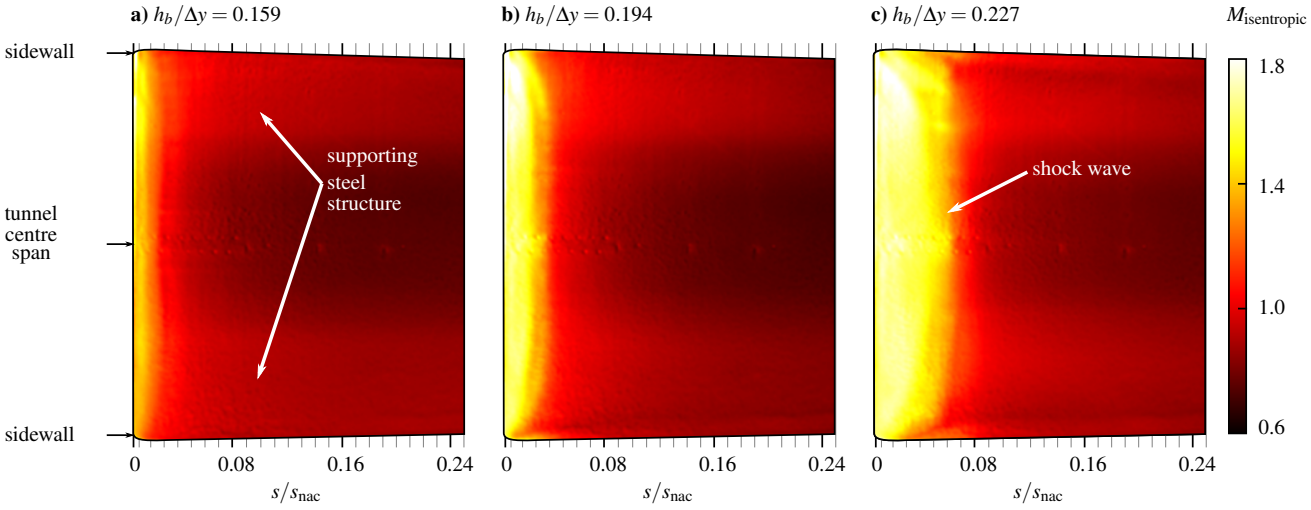


Figure 7: Isentropic Mach number distribution on the external nacelle surface obtained using PSP for different bump heights corresponding to variations in equivalent engine mass-flow rate.

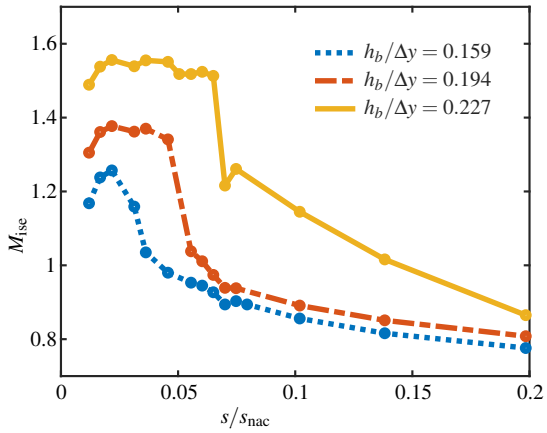


Figure 8: Pressure distribution on the external nacelle surface for different bump heights corresponding to variations in equivalent engine mass-flow rate.

butions pressure-sensitive paint (PSP) luminescence under ultraviolet excitation is recorded using a RaspberryPi camera module version 3 which has a Sony IMX708 sensor. In-situ calibration is performed using the static pressure taps, with reference images taken with the wind tunnel off. The expected uncertainty in these PSP measurements is roughly 3% although the error can be larger in regions where the underlying steel structure has thickness variations, changing the local thermal conductivity. The topology of the separated flow field is surveyed using surface oil-flow visualisation. This technique involves coating the tunnel floor with a mixture made from paraffin, finely-powdered titanium dioxide, oleic acid and lubricating oil. There is a small error due to oil-flow producing an inaccurate indication of separation location (by about 0.2 boundary-layer thicknesses = 0.6 mm) [9].

Boundary-layer profiles at $s/s_{\text{nac}} = 0.145$ are measured, for which the flow speed ($U$) is determined to an accuracy of 2% using two-component laser Doppler velocimetry (LDV). The flow is seeded with paraffin in the settling chamber with the seeding droplet diameter roughly $200-500$ nm [8]. Boundary-layer traverses are carried out with wall-normal resolution roughly 0.1 mm.

## 3. RESULTS

### 3.1 Effect of engine mass flow rate

The effect of variations in equivalent engine mass-flow rate is studied for nominal diversion windmilling conditions, i.e. $M_\infty = 0.65$ and a turbulent incoming boundary layer. For all three bump heights, $h_b/\Delta y = 0.159$, 0.194 and 0.227, the schlieren images in Fig. 5 show a dark region immediately upstream of the leading edge, which is related to the optical distortion caused by the strong local acceleration. The supersonic region can be visualised by the presence of weak waves emanating from the surface. The terminating normal shock appears in the schlieren images as a dark line approximately normal to the external fan cowl surface. The boundary layer downstream of the shock can be identified as a bright region which grows along the external nacelle surface.

As the bump height is increased, corresponding to a reduction in engine mass-flow rate, the supersonic region grows in size as the normal shock moves downstream. In addition, the SBLI structure progresses from an attached interaction with a smeared shock foot in Fig. 5a to a lambda-shock structure typical of a separated SBLI in Fig. 5c. The downstream boundary layer accordingly becomes thicker as the bump height is increased.

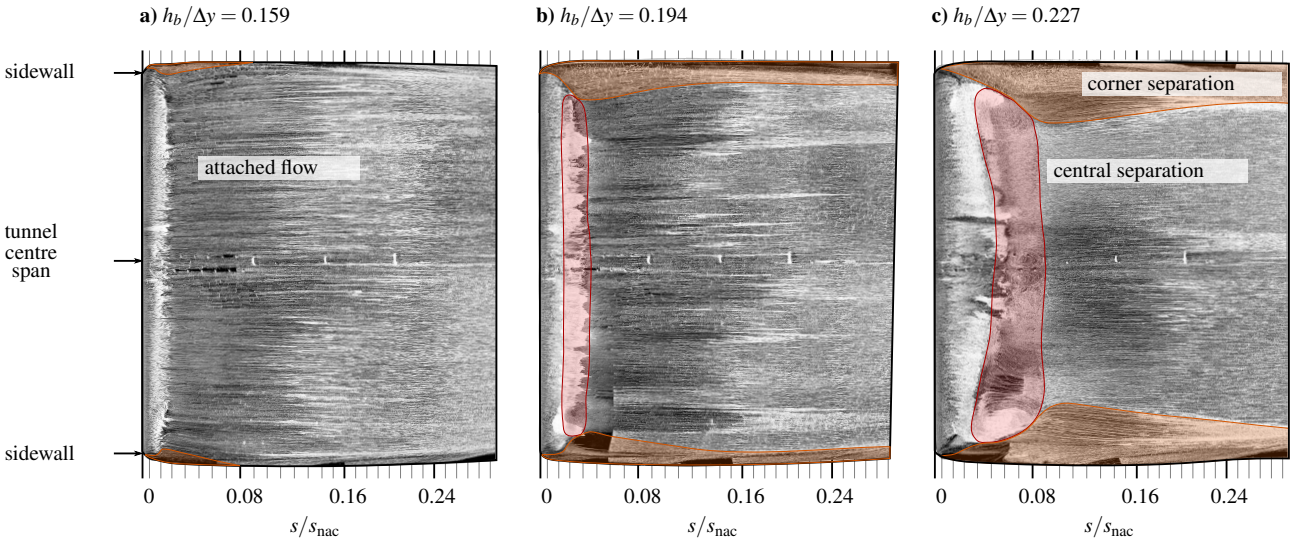


Figure 9: Surface oil-flow visualisation on the external nacelle surface for different bump heights corresponding to variations in equivalent engine mass-flow rate. Regions of corner separation are highlighted in orange and the main central separation is marked in red.

An explanation for the observed differences is related to the pressure distribution around the stagnation point on the internal surface, presented in Fig. 6. Although the stagnation point theoretically corresponds to $M_{\mathrm{ise}} = 0$, the profiles show an apparent minimum at $M_{\mathrm{ise}} = 0.05$. This Mach number is equivalent to $p/p_0 = 0.998$, which is within 0.2% of unity, compared to the stated uncertainty of 1%. Therefore, this measured minimum can be considered to reliably indicate the stagnation point location. As the bump height is increased, the stagnation point moves further inside the nacelle by approximately 0.005 $s_{\mathrm{nac}}$.

The shifted stagnation point affects the flow field on the nacelle's external surface, as demonstrated by the surface pressure distribution in Fig. 7. All three cases show a supersonic region terminating in a normal shock which is roughly uniform across the span of the tunnel. The apparent spanwise pressure variation downstream of the shock is not physical but is instead an artefact of local temperature variations caused by thermally-conductive steel supports underneath the resin sleeve, which increase the local error in PSP measurements. As the height of the bump increases and the stagnation point moves inside the nacelle, Fig. 7 shows that the supersonic region becomes larger. This effect is also evident in the surface pressure profile on the tunnel centre span (Fig. 8). This profile shows the shock wave move downstream from $s/s_{\mathrm{nac}} = 0.04$ to $s/s_{\mathrm{nac}} = 0.07$ as the bump height is increased. In addition the Mach number immediately upstream of the shock increases from 1.25 to 1.55, corresponding to a normal shock wave with greater strength.

There are two possible reasons for the more downstream, stronger stronger shock wave. One explanation is that the more downstream stagnation point for larger bump heights causes greater acceleration around the leading edge. As a result, the pressure at the beginning of the external fan cowl surface is lower, as evidenced in Fig. 8. Therefore, in order to meet the trailing edge pressure condition, a larger pressure rise is required. This condition corresponds to a stronger shock wave which tends to occur further downstream. However, the assumption in the above explanation that the trailing edge pressure is the same for all three cases may not be correct. Indeed, Fig. 8 shows differences in the pressure between the three cases up to at least $0.2s_{\mathrm{nac}}$. Therefore, an alternative explanation is that the changes are driven by differences in the trailing edge pressure condition. Namely, as the bump height is increased, the pressure at the trailing edge is larger and therefore a stronger shock is required. Whilst it is possible that both leading edge and trailing edge conditions are important, the lack of trailing-edge measurements prevents any definitive statement on the dominant mechanism at play.

The variations in shock wave strength consequently impact the separation behaviour, as measured using oil-flow visualisation (Fig. 9). The position of the shock wave is evident in 9a from an accumulation of oil corresponding to a sudden reduction in shear stress. Nevertheless the boundary layer remains attached across the majority of the tunnel span, except for a small region near the corners. For the intermediate bump height, Fig. 9b reveals separation across much of the span of the tunnel which extends roughly 0.025 $s_{\mathrm{nac}}$ in the streamwise direction. In addition, noticeable corner separation has begun to develop near the tunnel sidewalls. Finally, at $h_b/\Delta y = 0.227$, there appears to be more substantial separation which is also more three-dimensional in nature.

**a) raw velocity profile**

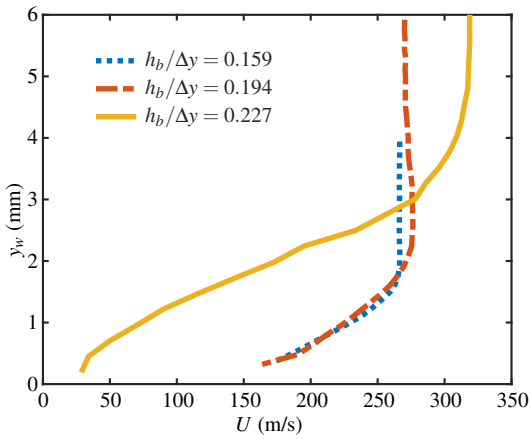


**b) scaled velocity profile**

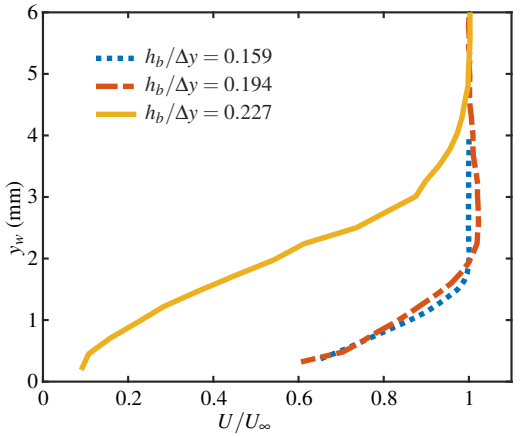


Figure 10: Boundary-layer profile at $s/s_{\text{nac}} = 0.145$ for different bump heights corresponding to variations in equivalent engine mass-flow rate: a) raw velocity profile; b) velocity values scaled by freestream velocity, $U_\infty$.

The streamwise separation length on the tunnel centreline has increased to 5% of the nacelle length and the corner separation has also grown in extent.

The effect of the development of separation on the external fan cowl boundary layer is clear from Fig. 10, which shows the velocity profile at $s/s_{\text{nac}} = 0.145$. Since the isentropic Mach number at this station is different for the three cases (Fig. 8), the freestream velocities in Fig. 10a are different. Therefore, a more useful comparison is obtained by scaling the velocity profiles by the freestream velocity, $U_\infty$, in Fig. 10b. Figure 10b shows that the boundary-layer thickness increases slightly from 1.6 mm to 2.1 mm as the flow goes from attached (Fig. 9a) to incipiently separated (Fig. 9b). However, Fig. 10b shows that the profile corresponding to Fig. 9c is significantly thicker (4.8 mm). This velocity distribution also exhibits substantial deviations from an equilibrium turbulent profile, suggesting that the boundary layer is still recovering after reattachment.

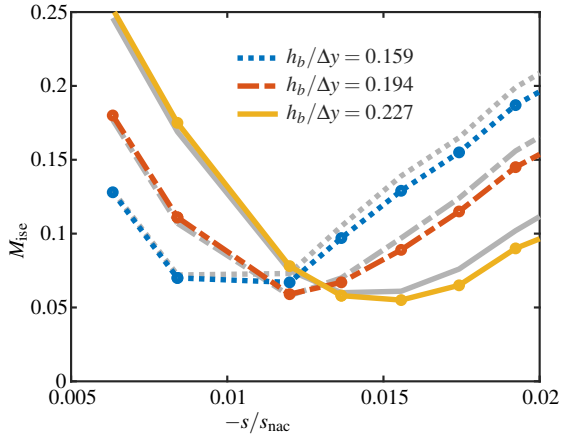


Figure 11: Pressure distribution on the internal nacelle surface around the stagnation point for different bump heights at a reduced entry Mach number, $M_\infty = 0.60$. The gray lines correspond to the equivalent profiles at $M_\infty = 0.65$.

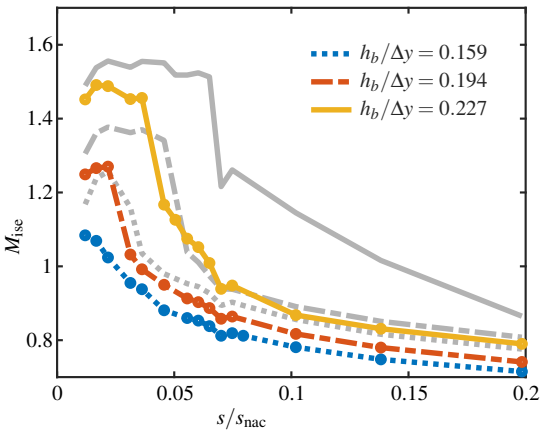


Figure 12: Pressure distribution on the external nacelle surface for different bump heights at a reduced entry Mach number, $M_\infty = 0.60$. The gray lines correspond to the equivalent profiles at $M_\infty = 0.65$.

## 3.2 Effect of Mach number

When the incoming Mach number is reduced from 0.65 to 0.60, Fig. 11 shows that the position of the stagnation point remains essentially unchanged. However, for all three mass-flow splits, the supersonic region is substantially smaller and the shock Mach number is roughly 10% lower than for $M_\infty = 0.65$ (Fig. 12). Indeed, for the smallest bump height, the shock has become so weak that it resembles a series of weak compression waves. These observations are consistent with the schlieren images in Fig. 13, which show a smaller supersonic region than Fig. 5. No shock wave at all is visible in Fig. 13a for $h_b/\Delta y = 0.159$. Meanwhile, the shock foot for the largest

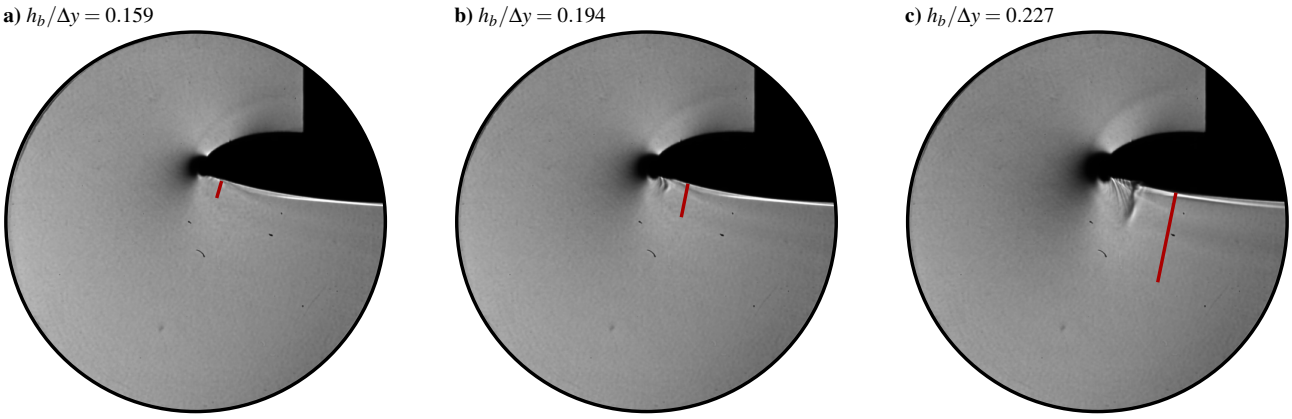


Figure 13: Schlieren images for different bump heights at a reduced entry Mach number, $M_\infty = 0.60$. The red lines correspond to the normal shock location at $M_\infty = 0.65$.

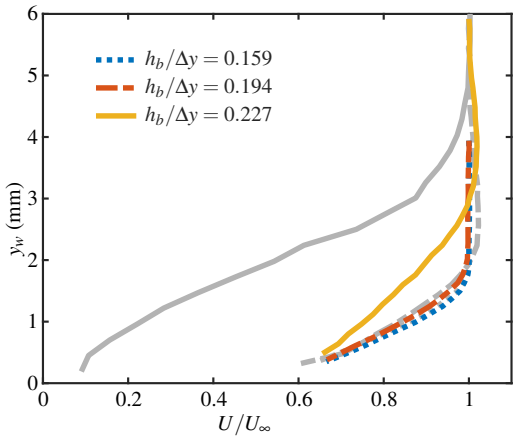


Figure 14: Scaled boundary-layer profiles at $s/s_{\text{nac}} = 0.145$ for different bump heights at a reduced entry Mach number, $M_\infty = 0.60$. The gray lines correspond to the equivalent profiles at $M_\infty = 0.65$.

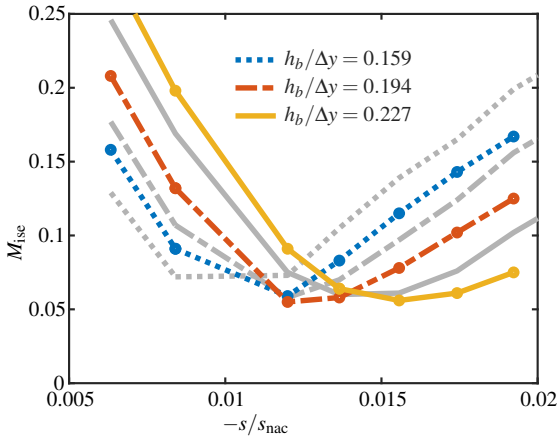


Figure 15: Pressure distribution on the internal nacelle surface around the stagnation point for different bump heights with a laminar incoming boundary layer. The gray lines correspond to the equivalent profiles for the turbulent case.

bump (Fig. 13c) has transformed from a lambda-shock structure to a smeared normal shock, suggesting that the flow field is now attached.

A reduced entry Mach number causes weaker shock waves because, for a given stagnation point, the same streamline curvature around the highlight produces roughly the same flow acceleration. Therefore, a lower entry Mach number corresponds to a reduced Mach number supersonic region and thus a weaker shock wave. Despite the weaker shock wave, there is almost no difference in the downstream boundary-layer profile for the smallest bump height in Fig. 14. This is likely because, for this mass-flow split, both the Mach 0.60 and Mach 0.65 cases correspond to the boundary-layer having always remained attached through the normal shock interaction. The boundary layer for the intermediate bump presents a small reduction in boundary-layer thickness compared to the Mach 0.65 case but is otherwise similar in profile. The most pronounced change, however, is for $h_b/\Delta y = 0.227$, where the boundary layer is about 30% thinner than at Mach 0.65 and has a much fuller profile. The reason for this is that the boundary layer now remains attached through the interaction with the weaker shock, and thus the downstream boundary layer is thinner and has more momentum.

## 3.3 Effect of boundary-layer state

At Mach 0.65, when the incoming boundary layer is laminar rather than turbulent, Fig. 15 shows that there is a small change in the position of the stagnation point, with the stagnation point approximately $0.001 s_{\text{nac}}$ further downstream than in the turbulent case. The reason for this

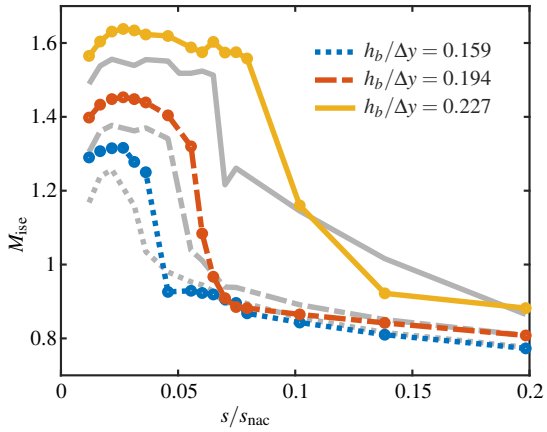


Figure 16: Pressure distribution on the external nacelle surface for different bump heights with a laminar incoming boundary layer. The gray lines correspond to the equivalent profiles for the turbulent case.

is not entirely clear, but is likely related to an interaction with the trailing-edge pressure condition. Whatever the reason for the shifted stagnation point, the greater flow acceleration around the leading edge causes a supersonic region with a higher Mach number (Fig. 16). As a result, the shock wave is stronger and located further downstream. Despite these differences, Fig. 16 suggests that, by $s = 0.2 s_{\mathrm{nac}}$, the pressures on the external fan cowl surface are equivalent to the values for the turbulent case.

The schlieren images in Fig. 17 are consistent with the pressure measurements. Compared to Fig. 5, the supersonic region is larger and the shock wave is further downstream. Interestingly, despite the shock wave being stronger in all cases, including $h_b/\Delta y = 0.227$, Fig. 17c contains no lambda-shock structure and there is no obvious separation. This is consistent with previous findings that laminar shock-induced separation can be relatively benign and very small in scale [7]. The downstream boundary layers in Fig. 18 are all considerably thinner than the equivalent turbulent cases. In cases with no flow separation, this is likely caused by the thinner incoming laminar boundary layer. On the other hand, cases which do feature flow separation also have a thinner boundary layer, which is consistent with the more benign separation noted in the schlieren images.

## 4. CONCLUSIONS

The development of ultra-high bypass ratio engines requires compact nacelles, and so it is becoming increasingly important to understand external fan cowl separation in off-design conditions. This paper presents an investigation into one such scenario, diversion windmilling, when the engine shuts down during the cruise phase of flight. These conditions are based on NASA CRM cruise $\alpha = 4.5$ degrees with the flight Mach number reduced from the cruise value to $M_\infty = 0.65$. Experiments are performed in a quasi-two-dimensional wind tunnel rig installed into a transonic blowdown wind tunnel, which has been carefully designed to replicate the flow physics from a full-scale nacelle. As the equivalent engine mass-flow rate is reduced, the stagnation point moves downstream inside the nacelle lip. The flow is therefore accelerated more severely around the nacelle leading edge, resulting in a higher-Mach number supersonic region on the external surface. The terminating normal shock therefore moves downstream and the shock Mach number increases from 1.25 to 1.55 over the mass-flow range studied. Across this range, the onset and growth of shock-induced boundary-layer separation is observed. As a result, the downstream boundary layer at roughly 15% of the chord length thickens by a factor of three.

When the incoming Mach number is reduced from 0.65 to 0.60, the flow field becomes more benign. The supersonic region features Mach numbers approximately 10% lower than the nominal Mach 0.65 condition, and so the normal shock is correspondingly weaker. As a result, no boundary-layer separation is detected over the mass-flow split range considered. There are negligible differences in the downstream boundary-layer profile for mild and moderate windmilling severity, where the boundary layer is attached or incipiently separated at $M_\infty = 0.65$. However, low engine mass-flow rates which feature well-developed separation at $M_\infty = 0.65$ are observed to exhibit a thinner boundary layer with greater momentum when the Mach number is reduced to 0.60.

A nacelle undergoing diversion windmilling at full scale is expected to experience a turbulent SBLI. However, this interaction can become transitional or laminar at Reynolds numbers only slightly less than the nominal conditions. If a laminar rather than turbulent boundary layer is encountered at Mach 0.65, the normal shock wave moves further downstream and becomes stronger. However, even for the lowest engine mass-flow rates studied, no substantial shock-induced separation can be detected and the boundary layer downstream of the interaction is substantially thinner than in the turbulent case.

The experiments provide some insight into the key mechanisms defining the diversion windmilling flow field, although some open questions remain. It is not clear whether the strength (and position) of the normal shock is governed primarily by the flow acceleration around the leading edge or by the trailing-edge pressure condition. Similarly, the precise reasons for the stagnation point shifting further inside the nacelle for a laminar versus turbulent boundary layer have not been determined. A key to answering these questions is the trailing edge pressure value, which cannot be easily measured in experiment. Therefore, computations of the wind tunnel flow path per-

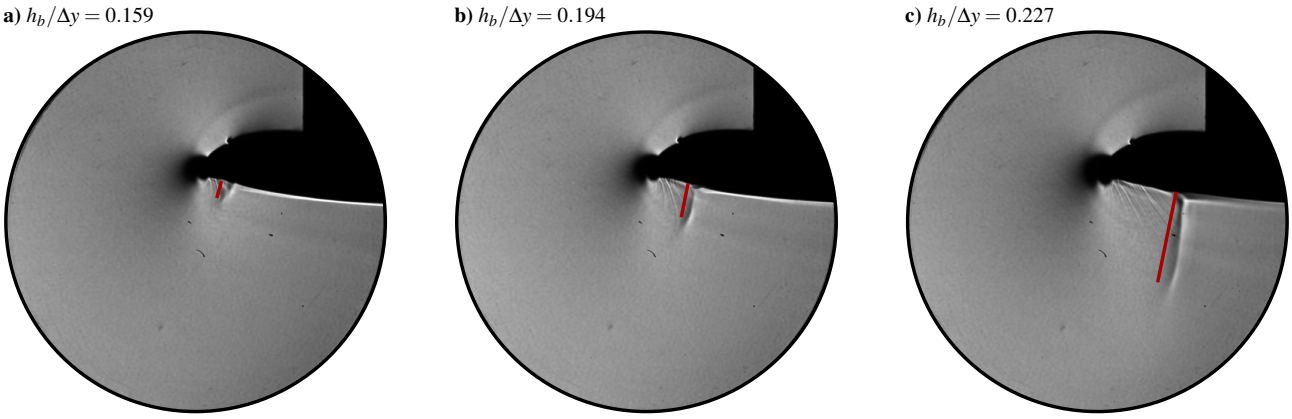


Figure 17: Schlieren images for different bump heights with a laminar incoming boundary layer. The red lines correspond to the normal shock location for the turbulent case.

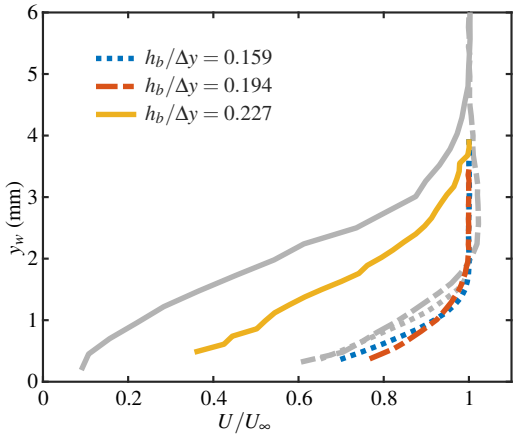


Figure 18: Scaled boundary-layer profiles at $s/s_{\text{nac}} = 0.145$ for different bump heights with a laminar incoming boundary layer. The gray lines correspond to the equivalent profiles for the turbulent case.

formed under the ODIN project will be used to provide the missing information. Comparisons of these simulations against the measurements will also provide valuable information on the capabilities of existing computational methods to reliably predict key flow parameters in diversion windmilling scenarios, as required to guide the design of UHBPR nacelles.

## ACKNOWLEDGEMENTS

This project has received funding from the Clean Sky 2 Joint Undertaking (JU) under grant agreement No 101007598. The JU receives support from the European Union's Horizon 2020 research and innovation programme and the Clean Sky 2 JU members other than the Union. The authors would like to thank D. Martin, A. Luckett and C. Costello for operating the blow-down wind tunnel. The authors are also grateful to N. Atkins and W. Davis for loan and assistance with the operation of the infrared thermography camera.

## REFERENCES

[1] B.J. Deneys Schreiner, F. Tejero, D.G. MacManus, and C. Sheaf. Robust aerodynamic design of nacelles for future civil aero-engines. In *Turbo Expo: Power for Land, Sea, and Air*, volume 84058, page V001T01A015. American Society of Mechanical Engineers, 2020.

[2] European Commission. FlightPath 2050: Europe's vision for aviation. Technical Report EUR 098 EN, Publications Office of the European Union, 2011.

[3] A. Magrini, E. Benini, H.-D. Yao, J. Postma, and C. Sheaf. A review of installation effects of ultra-high bypass ratio engines. *Progress in Aerospace Sciences*, 119:100680, 2020.

[4] W. Hoelmer, J.L. Younghans, and J.C. Raynal. Effect of Reynolds number on upper cowl flow separation. *Journal of Aircraft*, 24(3):161–169, 1987.

[5] K. Sabnis, L. Boscagli, A. Swarthout, F. Tejero Embuena, H. Babinsky, D. MacManus, and C. Sheaf. A wind tunnel rig to study the external fan cowl separation experienced by compact nacelles in windmilling scenarios. In *AIAA Scitech 2023 Forum, AIAA Paper 2023-1942*, 2023.

[6] A. Swarthout, D. MacManus, F. Tejero, J. Matesanz Garcia, L. Boscagli, and C. Sheaf. A comparative assessment of multi-objective optimisation methodologies for aero-engine nacelles. In *33rd Congress of the International Council of the Aeronautical Sciences*, 2022.

[7] A. Coschignano, N. Atkins, H. Babinsky, and J. Serna. Effect of Reynolds number on a normal shock wave-transitional boundary-layer interaction over a curved surface. *Experiments in Fluids*, 60(12):185, 2019.

[8] S.P. Colliss, H. Babinsky, K. Nübler, and T. Lutz. Vortical structures on three-dimensional shock control bumps. *AIAA Journal*, 54(8):2338–2350, 2016.

[9] L.C. Squire. The motion of a thin oil sheet under the steady boundary layer on a body. *Journal of Fluid Mechanics*, 11(2):161–179, 1961.

2023-03-29

# Experimental investigation of transonic external fan cowl separation

Sabnis, Kshitij

Association Aeronautique Astronautique de France

Sabnis K, Boscagli L, Babinsky H, et al., (2023) Experimental investigation of transonic external fan cowl separation. In: 57th 3AF International Conference on Applied Aerodynamics, 29-31 March 2023, Bordeaux, France

https://www.3af.fr/fr/agenda/57th-edition-of-the-3af-international-conference-on-applied-aerodynamics-2222